A variable-gap model for helium bubbles in nickel

Miroslav Fokt, Gilles Adjanor, Thomas Jourdan

HAL Id: cea-03507803
https://cea.hal.science/cea-03507803

Submitted on 3 Jan 2022

A variable-gap model for helium bubbles in nickel

M. Fokt[a,b], G. Adjanor[a,*], T. Jourdan[b]

[a]*Département Matériaux et Mécanique des Composants, EDF-R&D, Les Renardières, 77250 Moret-sur-Loing, France*
[b]*Université Paris-Saclay, CEA, Service de Recherches de Métallurgie Physique, 91191 Gif-sur-Yvette, France*

Abstract

In nuclear fission reactors, the amount of helium produced in materials by transmutation reactions at the end of the lifetime may reach several thousands of atomic parts per million (appm). Such high levels of helium production can impact the evolution of microstructures, particularly by forming helium bubbles. To better understand the role of helium on the stability of bubbles, a "variable-gap model" was parametrized with molecular dynamics (MD) calculations performed in nickel. This model predicts binding energies in a good agreement with MD values, especially for large bubbles. For very small bubbles, the influence of magic number sizes and faceting is more complex than can be described with the model. For these cases, it is proposed to use MD values directly.

Keywords: helium, bubbles, nickel, binding energy

1. Introduction

Helium production and formation of bubbles play an important role in microstructure evolution under neutron irradiation [1]. In fission reactors, helium is produced by transmutation reactions mostly from nickel interacting with thermal neutrons. Under such conditions, material is subjected to a neutron

---

*Corresponding author

Email addresses: `miroslav-m.fokt@edf.fr` (M. Fokt), `gilles.adjanor@edf.fr` (G. Adjanor), `thomas.jourdan@cea.fr` (T. Jourdan)

flux which causes substantial changes in the microstructure. High energy neu-
trons, so-called *fast* neutrons, cause displacements of atoms, creating vacancy-
interstitial (or Frenkel) pairs (FPs). Point-defects from FPs cluster into self-
interstitial atoms (SIAs) clusters and voids. Lower energy neutrons, so-called
thermal neutrons, may interact with nickel atoms and form helium by trans-
mutation of nickel into iron. Another less significant source of He is boron,
contained in steels in small amounts as impurities. The amount of helium pro-
duced is usually expressed in terms of a helium-to-displacement per atom ratio
(He/dpa). Helium production ranges in ASS from 0.1-0.8 appm He/dpa in
fast breed reactors [2, 3], to about 10 appm He/dpa [4, 5, 6, 2] in pressurized
water reactors (PWR), and about 70 He appm/dpa in HFIR [7, 8]. In nickel
based alloys, He production can reach more than 300 appm/dpa in CANDU
reactors [9].

As a noble gas, helium is insoluble in the material, and in an interstitial
position it can move easily in the bulk [10]. It is therefore quickly captured
by sinks - mostly bubbles, but also other defects such as dislocations and grain
boundaries [11, 12, 13, 14]. Theoretical calculations showed that small voids
in metals are metastable [15], and that the presence of gaseous atoms would
explain their experimental evidence [16]. Crucial ideas on modelling helium
accumulation in metals were reviewed by Trinkaus et al. [17]. Helium in bubbles
increases internal pressure, and therefore thermal stability, by reducing vacancy
emission. This should favour bubble nucleation, but the reality is more complex
and under irradiation, factors favouring nucleation may lower the growth of
bubbles.

Growth kinetics of bubbles must be modelled more accurately and quanti-
tatively with kinetic Monte-Carlo [18, 19] or with a rate equations approach
such as cluster dynamics (CD) [20, 21, 22, 23, 24, 25, 26]. In a CD approach,
emission coefficients are calculated using binding energies, and they describe at
which rates vacancies, SIAs and helium atoms are emitted from bubbles.

Such methods require precise parametrization of binding energies at arbi-
trary large sizes, and it is thus particularly important to have a model [27, 28, 29]

2

that calculates binding energy over a wide range of sizes and He densities, specifically in terms of the helium-to-vacancy (He/vac) ratio, which significantly varies under different experimental conditions. The He production rate varies in different materials under different neutron spectra, and the stability of bubbles can be quite different for different He/vac ratios.

In this work, a variable-gap model predicting binding energies to helium bubbles, initially developed for body-centered cubic (BCC) iron [27], is adapted based on data from molecular dynamics (MD) simulations in nickel. Nickel can provide an important foundation on the behaviour of helium bubbles in Ni-based alloys [30], but also Fe-based FCC alloys, as behavior of He is expected to be similar to Ni [31, 32]. A particular challenge arises from using nickel to simulate defect clusters at finite temperatures, as a recent combined density functional theory and MD simulation study shows that voids are unstable [33].

Section 2 reviews the description and assumptions of the energy model. The description of simulation settings is presented in section 3, followed by the adaptation of the model on obtained MD data in section 4, commenting on several differences and limitations compared to the Fe model. Then, equilibrium helium density predicted by the model is compared with available experimental data.

2. Energy model

A bubble that contains m vacancies and n helium atoms is labeled in parentheses (m, n). The main assumption is that a void has a spherical shape [34, 35] and that repulsion between helium and metal atoms is modeled as a variable-size gap between them [27]. The free energy of a bubble (m, n) is a sum of three different contributions: elastic energy of Ni atoms around the bubble $F_{\text{Ni-Ni}}(m, n)$, interaction of He and Ni atoms $F_{\text{Ni-He}}(m, n)$, and energy of helium atoms $F_{\text{He-He}}(m, n)$ described with an equation of state (EOS):

$$F^{\text{f}}(m, n) = F_{\text{He-He}}(m, n) + F_{\text{Ni-He}}(m, n) + F_{\text{Ni-Ni}}(m, n). \qquad (1)$$

We can define

$$\Delta F^{\mathrm{f}}(m,n) = F^{\mathrm{f}}(m,n) - F^{\mathrm{f}}(m,0), \tag{2}$$

where $F^{\mathrm{f}}(m,0)$ is the surface free energy, so

$$\Delta F^{\mathrm{f}}(m,n) = F_{\text{He-He}}(m,n) + F_{\text{Ni-He}}(m,n) + \Delta F_{\text{Ni-Ni}}(m,n), \tag{3}$$

where $\Delta F_{\text{Ni-Ni}}(m,n)$ is due to the surface relaxation. We assume that because of the gap, the helium content will have no effect on the surface energy itself, but the gap will induce stretching of surface atoms arising from an elastic effect accounted in $\Delta F_{\text{Ni-Ni}}(m,n)$. Then, $\Delta F^{\mathrm{f}}(m,n)$ can be defined as the formation free energy of the bubble.

The binding energy of a vacancy (V), an SIA (I), or a helium (He) atom is then calculated using formation energy $F^{\mathrm{f}}(m,n)$ as

$$F_{\mathrm{V}}^{\mathrm{b}}(m,n) = F_{\mathrm{V}}^{\mathrm{f}} + F^{\mathrm{f}}(m-1,n) - F^{\mathrm{f}}(m,n), \tag{4}$$

$$F_{\mathrm{I}}^{\mathrm{b}}(m,n) = F_{\mathrm{I}}^{\mathrm{f}} + F^{\mathrm{f}}(m+1,n) - F^{\mathrm{f}}(m,n), \tag{5}$$

$$F_{\text{He}}^{\mathrm{b}}(m,n) = F_{\text{He}}^{\mathrm{f}} + F^{\mathrm{f}}(m,n-1) - F^{\mathrm{f}}(m,n), \tag{6}$$

where $F_{\mathrm{V}}^{\mathrm{f}}$, $F_{\mathrm{I}}^{\mathrm{f}}$, and $F_{\text{He}}^{\mathrm{f}}$ are the formation energies of vacancy, SIA, and helium atom in a tetrahedral position, respectively. Parameters for these three terms were fitted on data extracted from MD simulations performed in face cubic centered (FCC) nickel using LAMMPS code [36], and the potentials to describe each interaction were: Bonny [37] for Ni-Ni, Torres for Ni-He [10], and Beck potential for He-He [38].

For fitting purposes, we assume that the function that sums up three different free energy contributions of the bubble is found as the minimum of the following function:

$$\Delta \Phi^{\mathrm{f}}(m,n,r_{\text{He}},r_V) = \Phi_{\text{He-He}}(n,r_{\text{He}}) + \Phi_{\text{Ni-He}}(n,r_{\mathrm{V}}-r_{\text{He}}) + \Delta \Phi_{\text{Ni-Ni}}(m,r_{\mathrm{V}}), \tag{7}$$

where r_{He} and r_V are helium's and the void's radii, respectively (Fig. 1). He-He interactions tend to maximize r_{He} while the $\Phi_{\text{Ni-Ni}}$ opposes to the increase of r_{V}.
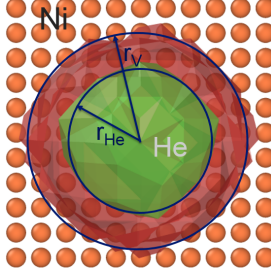
4

Figure 1: A typical snapshot of actual MD simulations. For visibility, helium atoms are hidden and replaced by the location of the surface of helium atoms (in green). The surface Ni atoms are also replaced by a calculated surface (in red). The structure is visualized using OVITO software [39] and *Construct surface mesh* modifier. The gap $r_{\text{Ni-He}}$ is the difference between the void's radius r_V and helium's radius r_{He}.

The minimum of the function $\Delta\Phi^{\text{f}}(m, n, r_{\text{He}}, r_V)$ (Eq. 7) with respect to r_{He} and r_V under the constraint $r_{\text{He}} < r_V$ will be equal to the formation free energy of a bubble $\Delta F^{\text{f}}(m, n)$ defined in Eq. 3. In this work we adapt this model to bubbles in Ni, using MD simulations to parametrize each term of Eq. 7, as described in the following sections.

2.1. He-He interaction

A possible way to describe the interaction energy of helium atoms in a bubble is with an EOS in terms of bulk atoms with a surface correction. An alternative approach used by Jelea [40] alters a bulk helium virial EOS by introducing a spherical confinement volume inside the bubble that accounts for the (repulsive) effects of the surface.

In this model, He-He interaction energy is described by Vinet EOS [41]. It was noted that alternative equations of state might be used for specific cases, but the fundamental behaviour doesn't change dramatically [42].

Bulk He atoms are identified using Voronoi volumes. For each helium atom, its Voronoi volume is calculated with Voronoi's tessellation for two cases - with and without Ni atoms. If the change of Voronoi's volume is negligible, an atom is considered a bulk atom. The Voronoi volume of helium can be computed for

a bubble with a minimum of 5 helium atoms, and for a bubble containing a bulk atom with a minimum of 15 helium atoms. The mean volume of helium v_{He} is computed as an average Voronoi volume of He bulk atoms. The total energy of He-He interactions extracted from MD runs at 0K is plotted in Figure 2 as a function of mean helium volume and compared with expression

$$e_{\text{He-He}}^{\text{bulk}}(v_{\text{He}}) = \int_{v_{\text{He}}}^{v_\infty} p_0 \mathrm{d}v, \tag{8}$$

which describes helium bulk energy as an integral of the pressure term p_0 at
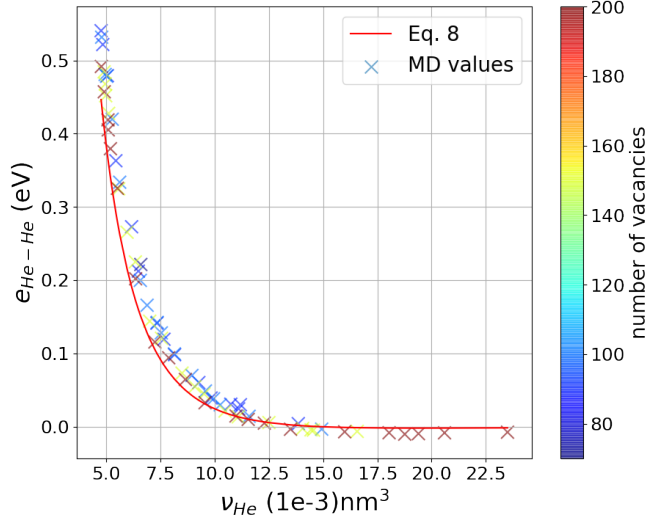

Figure 2: Energy of helium bulk atoms due to He-He interactions of different bubbles sizes and He to vacancy ratios, as a function of the mean He volume. MD values (crosses) are compared to Eq. 8 (solid line). Coloring corresponds to the number of vacancies in the bubble. (For interpretation of the references to colour in this figure legend, the reader is referred to the web version of this article.)

0K from the mean bulk helium volume v_{He}, up to infinite dilution. Vinet EOS

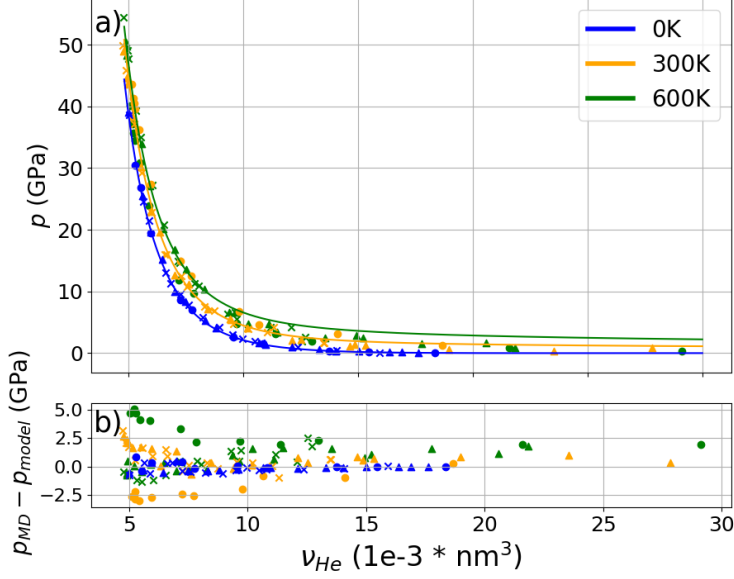$$p_0 = \frac{3K_0}{X^2}(1 - X)\exp(\eta_0(1 - X)), \tag{9}$$

6

Figure 3: a) internal pressure in bulk helium with respect to average bulk helium volume, model (solid lines) compared to the values extracted from MD (points), b) the difference between the model and MD values at the following temperatures: 0 (blue), 300 (orange), and 600 K (green), for different bubble sizes (crosses: $n = 100$; triangles: $n = 150$, and circles $n = 200$). (For interpretation of the references to colour in this figure legend, the reader is referred to the web version of this article.)

where

$$X = (\frac{v}{v_0})^{1/3}, \eta_0 \frac{3}{2}(K'_0 - 1), \tag{10}$$

was used with the same parameters as in [27] ($v_0 = 1.951 \cdot 10^{-2}$ nm^3, $K_0 = 1.497$ eV/nm^3, and $K'_0 = 8.465$) and it was verified that Eq. 8 gives reasonable results compared to the MD data (Figure 2).

One can express the ratio between energy of all atoms and bulk helium atoms due to He-He interaction with the help of the surface correction parameter α:

$$\frac{e_{\text{He-He}}}{e_{\text{He-He}}^{\text{bulk}}} = 1 - \frac{\alpha}{n^{1/3}}. \tag{11}$$

7

To take into account the effect of temperature, a temperature-dependent term [29] is added to the 0K expression for pressure. The model was validated by checking pressure at $T = 0K$, 300K, and 600K (Fig. 3). Average pressure for He bulk atoms was calculated using LAMMPS' stress tensor described in [43]. The bulk free energy can be written as

$$f_{\text{He-He}}^{\text{bulk}}(v_{\text{He}}) = \int_{v_{\text{He}}}^{v_\infty} p \, \mathrm{d}v + f_{\text{He-He}}^{\text{ideal}}(v_\infty). \tag{12}$$

A sufficiently high value of v_∞ was chosen so that the ideal gas approximation is valid ($p = 10^3 \text{Pa}$) and so that the free energy of an ideal gas $f_{\text{He-He}}^{\text{ideal}}(v_\infty)$ is valid.

Helium radius is deduced from a sphere with a volume equal to the number of He atoms multiplied by the average helium volume v_{He}

$$n v_{\text{He}} = \frac{4}{3} \pi r_{\text{He}}^3, \tag{13}$$

so the final term of the free energy that corresponds to He-He interactions expressed as a function of He radius r_{He} has the following form:

$$\Phi_{\text{He-He}}(n, r_{\text{He}}) = n f_{\text{He-He}}^{\text{bulk}}(r_{\text{He}}) \left(1 - \frac{\alpha}{n^{1/3}}\right). \tag{14}$$

2.2. Ni-He interaction

In our approach, following Jourdan and Crocombette [27], Ni-He interaction energy is derived directly from the potential φ and positions of atoms over all Ni-He pairs

$$E_{\text{Ni-He}}(n, m) = \sum_{\text{Ni-He interaction pairs}} \varphi(r_i). \tag{15}$$

Most of the energy comes from the interaction at the surface. In this model, it is convenient to express nickel-helium interaction energy as a function of *characteristic* distance $r_{\text{Ni-He}}$ such that

$$\Phi_{\text{Ni-He}}(n, r_V - r_{\text{He}}) = n^{2/3} g(r_{\text{Ni-He}}) \varphi(r_{\text{Ni-He}}), \tag{16}$$

8

where g is a function that will be defined in section 4.2, and with $r_{\text{Ni-He}}$ being defined as the weighted radius of Ni-He pair interaction

$$r_{\text{Ni-He}} = \frac{\sum r_i \varphi(r_i)}{\sum \varphi(r_i)}. \tag{17}$$

2.3. Ni-Ni interaction

It was assumed that Ni-Ni contribution comes from matrix bulk relaxation. We generalized the formula based on Eshelby's inclusion for a spherical void in an isotropic material, to an anisotropic material (see Appendix B), leading to the following expression for the elastic energy around a void of theoretical radius r_{V}^{0} [1] due to surface relaxation $r_{\text{V}} - r_{\text{V}}^{0}$:

$$\Delta\Phi_{\text{Ni-Ni}}(m, r_{\text{V}}) = 8\pi\mu r_{\text{V}}^{0}(r_{\text{V}} - r_{\text{V}}^{0})^2, \tag{18}$$

where μ is an effective shear modulus (see Appendix B), and the difference $\Delta r = r_{\text{V}} - r_{\text{V}}^{0}$ reflects the void's radius change due to helium pressure. The Δr values were directly extracted from MD, with the algorithm that is described in Appendix A. The effect of helium is hidden in the r_{V} value, which is the actual radius of the bubble.

3. Setting up the simulation

Simulations were performed in a simulation box of a size $30a_0 \times 30a_0 \times 30a_0$ (with $a_0 = 0.352$ nm). It was verified that the box size is sufficient to avoid periodic boundary condition interaction for defects up to 200 vacancies in size. Potentials used are mentioned in section 2.

Initially, MD should have been used to explore energy landscape of bubbles, but it was found that in the case of nickel, bubbles are not thermodynamically stable below a given He/vac ratio, and transform into stacking fault tetrahedra

---

[1]Theoretical value r_{V}^{0} is deduced from the void's volume as the number of vacancies n multiplied by atomic volume V_{at}.

(SFT)-like structures. This transformation was observed in FCC Cu during ac-
celerated MD (parallel-replica dynamics) of vacancy clusters [44]. It was also
observed using first-principles calculations based on density-functional theory
(even after much shorter times - ps) at temperatures up to 1000K in Ni, whereas
at 0K voids are more stable than SFTs [33]. These results suggest the impor-
tance of possible temperature effects in concluding thermodynamic stability of
vacancy clusters in FCC metals. Although quite general in irradiated pure fcc
metals, the presence of SFTs is much more controversial for more complex alloys
such as 304 and 316 ASS [45], which are used in typical applications.

As our goal is to determine formation energies of bubbles with helium, we
want to simulate spherically shaped bubbles, and thus be ensured that trans-
formation into SFT due to thermal activation did not occur.

Firstly, spherical voids (up to the size of 200 vacancies) were created, by a
sequence of removing atoms and relaxing structures with the conjugate gradient
(CG) algorithm. For voids up to 20 vacancies, atoms with the highest potential
energy were removed. For bigger voids, to keep the spherical shape of voids,
atoms closest to the center were removed. We are aware of the fact that this
particular process of creating void structures can place potential energy at some
point (local minimum) of energy landscape that does not have to be the global
minimum, but it was considered sufficient, as thermostatting at some higher
temperature would lead to transformation towards SFT. Afterwards, helium
atoms were inserted into voids, filling them with various helium content, from 0
to a He/vac ratio equal to 2.5, followed by CG relaxation. This was the starting
configuration for the actual MD. For bubbles with more than 150 vacancies and
a He/vac ratio bigger than 2.5, emission of SIAs was observed.

The conditions were then set to allow for thermostatting at moderate tem-
peratures. After the atoms' velocity scaling reached the temperature of 100K[2]
(50 000 steps by 0.2 fs in NVT ensemble), the system switched to NVE ensemble

---

[2]Higher temperatures 300K and 600K indicated structure changes, and so some effect of
thermal stability

¹⁷⁵ for the same number of steps[3]. Every 500 time steps, positions of atoms were
¹⁷⁶ saved and later relaxed with CG. Out of all of the relaxed structures from the
¹⁷⁷ MD run, the one with the lowest energy was chosen.

¹⁷⁸ The effect of helium on the bubble's radius was extracted from the lowest
¹⁷⁹ energy configuration, comparing it with the radius of the bubble that had He
¹⁸⁰ atoms removed and subsequently was relaxed.

¹⁸¹ 4. Adaptation of the model to the FCC case

¹⁸² *4.1. He-He interaction*

¹⁸³ It was verified that the bulk part of helium energy agrees with the values
¹⁸⁴ from MD. However, it was found that the value of α (surface correction term)
¹⁸⁵ is equal to 2.038 (Fig. 4), which is higher than in the previous studies in BCC
¹⁸⁶ Fe by Jourdan [27] ($\alpha = 1.354$) and by Morishita [18]($\alpha = 1.37$). The value
¹⁸⁷ 1.37 was derived from the number of deficit bonds for a spherical FCC cluster
¹⁸⁸ in the limit of a large cluster size [46]. Since the bubble's surface is faceted,
¹⁸⁹ the different value of α may point to an effect of the bubble's shape on Ni-He
¹⁹⁰ interaction and thus on the surface correction term.

¹⁹¹ *4.2. Ni-He interaction*

¹⁹² A function that accounts for the change in the number of Ni-He bonds as
¹⁹³ $r_{\text{Ni-He}}$ changes,

$$g(r_{\text{Ni-He}}) = \frac{g_0}{\exp(\frac{r_{\text{Ni-He}}-r_0}{\Delta r}) + 1}, \tag{19}$$

¹⁹⁴ was fitted on the MD data (Fig. 5), yielding $g_0 = 12.53$, $r_0 = 3.7$ nm, and
¹⁹⁵ $\Delta r = 0.22$ nm. Compared to α-Fe, Ni-He interaction energy is lower for bubbles
¹⁹⁶ with a gap smaller than 0.28 nm, and higher for bubbles with a gap bigger than
¹⁹⁷ 0.28 nm. Standard deviation of the distribution $P(r)\varphi(r)$ (radial distribution
¹⁹⁸ function $P(r)$ represents the density of bonds, $\varphi(r)$ is the interatomic potential
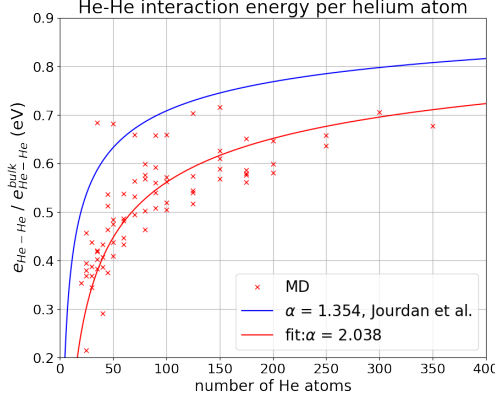
---

[3]No transformation to SFT was observed

Figure 4: Ratio of energy of all helium and bulk helium atoms due to He-He interactions of different bubbles sizes as a function of number of the helium atoms n in the bubble, with its fit for surface correction in the current study (red line) compared to a value in ref [27] (blue line).

for Ni-He) can be used to account for spread of the density of bonds in terms of distance around $r_{\text{Ni-He}}$:

$$\sigma(r_{\text{Ni-He}}) = \sigma_1 r_{\text{Ni-He}} + \sigma_0, \tag{20}$$

with fitted parameters $\sigma_1 = -0.721$ and $\sigma_0 = 2.931$ nm (see section 4.4).

4.3. Ni-Ni interaction

Eq. 18 describing matrix bulk relaxation was compared to energies from MD. In practice, two quantities can be extracted from MD - atomic strain tensor (comparing positions of Ni atoms with a case where He atoms were removed and bubble was relaxed using CG, later used to compute elastic energy), or the change in total Ni-Ni interaction energy. The former estimates the elastic energy and has the advantage of having information on the contribution of each atom (relaxed elastic energy due to He atoms in the bubble). The latter collapses into one macroscopic value. Unfortunately, none of these were able to capture the exact trend of the energy with respect to the Δr value, as shown in Fig. 6.
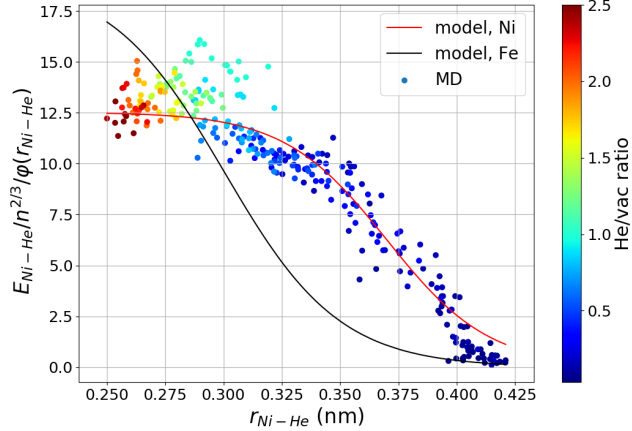
12

Figure 5: Normalized Ni-He interaction energy. Values from MD (circles) are fitted to Eq. 19 for nickel (red solid line), compared with α-Fe (black solid line) [27]. Coloring refers to helium to vacancy ratio. (For interpretation of the references to colour in this figure legend, the reader is referred to the web version of this article.)

Further analysis of bubbles' surfaces revealed non-negligible faceting typical of octahedral-like shapes, as experimentally observed in FCC alloys [1, 47, 48]. This shows that the assumption of sphericity in this study was not precisely met. To be more quantitative, we may correlate this with the difference between equilibrium crystal shapes given by the Wulff construction at $T = 0$K of Fe and Ni, using a ratio between surface and volume $\eta = A/V^{2/3}$. A reference value for a sphere is $\eta_{\text{sphere}} = (36\pi)^{1/3} = 4.83$, while for $\alpha-$Fe it is $\eta_{\text{Fe}} = 4.94$, and $\eta_{\text{Ni}} = 5.18$ for nickel [49]. In BCC, equilibrium shape consists of more higher order planes (more spherical), whereas in FCC it mostly consists of {111} and {100} planes, having less spherical shape due to the low surface energy of these planes [50].

An algorithm described in Appendix A was used to detect the surface's orientation by finding the closest crystallographic direction to its normal. A majority of surfaces were detected as {111} and {100} planes. Small voids were mostly composed of {111} planes/facets, while with increasing size, the

²²⁷ surface grew in complexity. The shape looks like an experimentally observed
²²⁸ truncated octahedron. It is expected that with increasing size, the surface will
²²⁹ be composed of numerous facets of higher order planes, as shown by the Wulff
²³⁰ construction for equilibrium crystal shape of Ni using values for surface energies
²³¹ calculated by DFT [33]. Figure 6 (b) shows that the discrepancy is linked to the
²³² surface orientation and thus to the faceting. Although the discrepancy for some
²³³ configurations seems to be in the order of tens of eV, it should be noted that the
²³⁴ model is used to calculate the binding energies (Eq. 4- 6), and therefore only
²³⁵ the increment of the Ni-Ni part (Eq. 18) of the formation energy is relevant, as
²³⁶ r_V varies due to the emission of a vacancy or a helium atom. The error of this
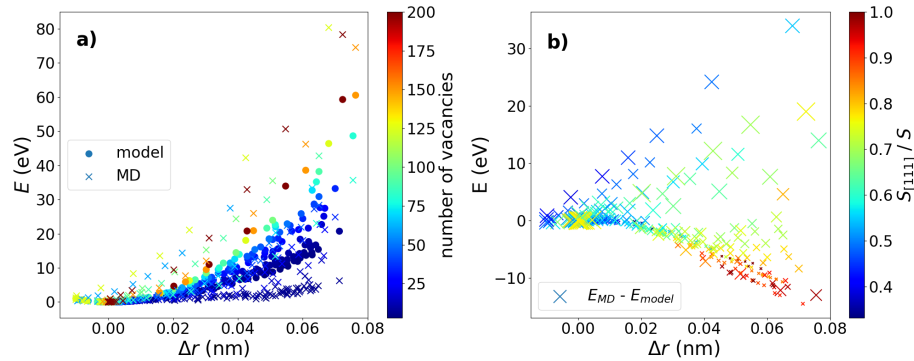²³⁷ quantity is much lower.

Figure 6: (a) Energy due to the elastic relaxation (spheres) and change in the energy extracted from MD (crosses) with respect to an increment of radius (coloring: bubble size), and (b) its difference (coloring: ratio of bubbles' surfaces oriented in [111] direction with respect to overall surface, marker size: number of vacancies). (For interpretation of the references to colour in this figure legend, the reader is referred to the web version of this article.)

²³⁸   In order to better understand the effect of He on a bubble's surface orien-
²³⁹ tation, further investigation is necessary. The sizes of bubbles in this study
²⁴⁰ are at the resolution limit of transmission electron microscope (TEM), and it is
²⁴¹ challenging to identify bubbles bellow 1nm. Furthermore, at such small sizes,
²⁴² specimens might not be suitable for further analysis to determine helium density
²⁴³ in the bubble with electron energy loss spectroscopy (EELS) technique [51], and
²⁴⁴ in experiments it is assumed that pressure induced by helium cause spherical

14

shapes of cavities [52]. To verify this, it would be necessary to introduce more helium in bubbles exceeding a He/vac ratio of 2.5, but it was found that these configurations of helium bubbles in nickel using the current set of potentials are not stable at finite temperatures.

4.4. Binding energy

Until now, particular free energy contributions to the model have been fitted with physical values calculated from MD. To minimize the difference between binding energies predicted by the model and the values from MD, parameters β and r_s in the equation for bubble radius were introduced, adding some degrees of freedom:

$$r_\text{V} = r_\text{He} + r_\text{Ni-He} - \beta\sigma(r_\text{Ni-He}) - r_\text{s}. \tag{21}$$

The best fit of β and r_s with emphasis on bubbles containing a higher number of vacancies and a lower number of He atoms was found for values $r_\text{s} = 0$ and $\beta = 1.05$.

The final comparison of helium and vacancy binding energies is shown in Figure 7 (color scale indicates the number of vacancies in the bubble). The model predicts binding energies accurately, except for very small sizes (number of vacancies ≤ 15), where the model assumptions are weakly met. For small clusters, shapes are strongly faceted and energetics is non-monotonic due to magic number sizes with high symmetry. Particularly more pronaunced effect of facetting is also for bubble containing 80 vacancies, and for various bubble sizes above 2 He/vac ratio, which cause higher discrapancy between binding energy vaules from the model and from MD. However, when the model is implemented in larger scale CD simulation codes, MD values for small clustes can be used directly.

5. Equilibrium helium density

In metallic materials, helium density in bubbles can be measured using different experimental techniques. Each of these techniques that are used for charac-
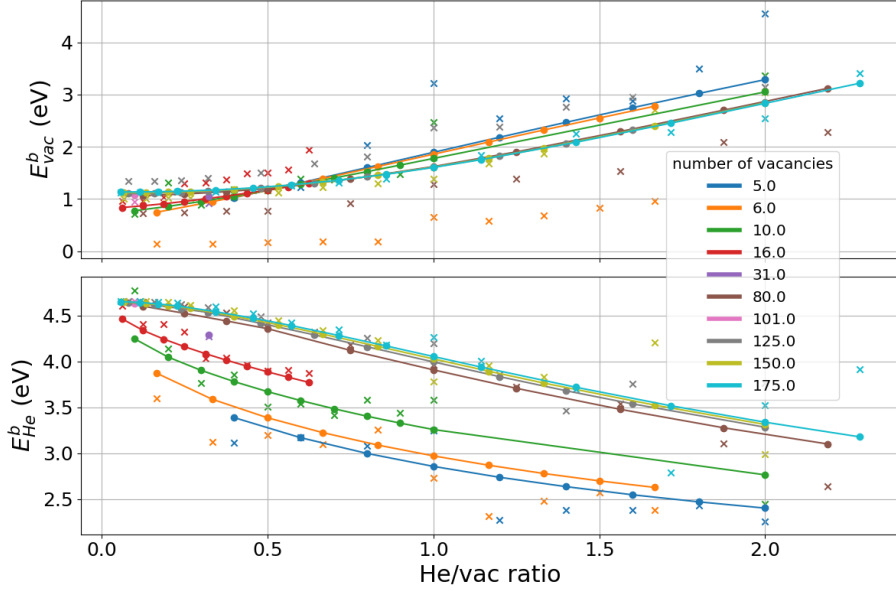
Figure 7: Comparison of vacancy (top) and helium (bottom) binding energies extracted from MD (symbols) with the model predictions (lines) as a function of helium to vacancy ratio for various bubble sizes. (For interpretation of the references to colour in this figure legend, the reader is referred to the web version of this article.)

terization of nanometric sized defects include some non-negligible uncertainity, especially for smaller radii and higher He densities.

Ameranda et al. [53] used positron-annihilation spectroscopy (PAS) to measure helium density in pure nickel with homogeneously implanted He as a function of the temperature during isochronal annealing.

Qiang-Li et al. [54] used a contrast variation method of small angle neutron scattering (SANS) combined with TEM to extract information on the bubble structure in Ni, implanted with 1200 appm helium at room temperature, and annealed at various temperatures between 820K and 1170K. Torres et al. [30] used electron energy loss spectroscopy (EELS) combined with scanning TEM to characterize Ni-alloy Inconel X-750, irradiated up to 80 dpa in a high thermal flux at 300-330°C and 25000 appm helium [9, 55]. Walsh et al. [56] measured He bubbles in Ni-based PE16 alloy iradiated during operation in a nuclear reactor

at a temperature of about 550°C with EELS and TEM.

In some studies [57, 58, 59], measured values are compared to the "$p = 2\gamma/r$" law, where γ is the surface energy, p is pressure in the bubble, and r its radius, which is valid for bubbles in thermal equilibrium. In refs [54, 53], measured values were found almost 3GPa larger than values from the "$p = 2\gamma/r$" law, stating that the vacancy supply is too small to relax the bubbles to the equilibrium. The fact that He was (pre)implanted with α-particles certainly plays a role. The equilibrium helium density for each void size can be calculated as a He/vac ratio where the vacancy binding energy is approaching vacancy formation energy (the chemical potential of a vacancy inside a bubble is $\mu_V = F^f(m,n) - F^f(m-1,n) = F^f(1,0) - F_V^b(m,n)$). The variable-gap model predicts lower He density for small bubbles than the "$p = 2\gamma/r$" law, converging to the same values with increasing radius r_V^0 (Fig 8). Small bubbles, which appeared to be nearly at equilibrium in refs [54, 53], when compared to the "$p = 2\gamma/r$" law, are in fact in overpressurized as other bubbles if the variable-gap model is considered.
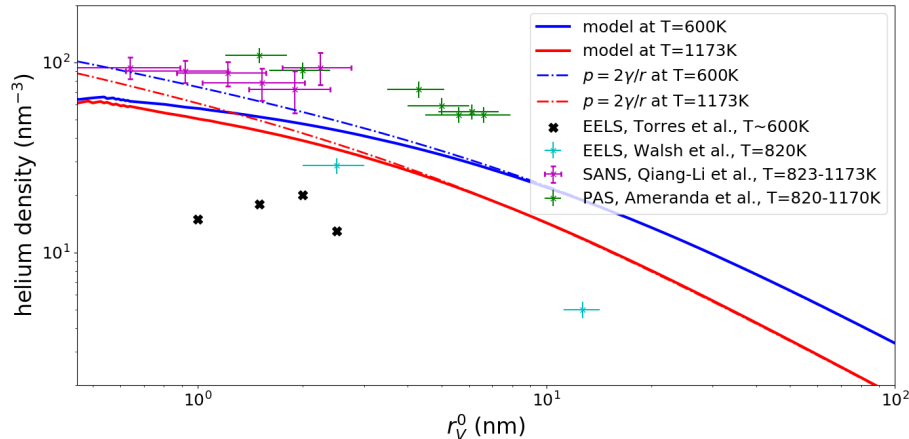

Figure 8: Helium density in bubbles at thermal equilibrium as a function of bubbles' unrelaxed radius r_V^0. Solid lines: the variable-gap model in Ni, dash-dot lines: "$p = 2\gamma/r$" law with Trinkaus' EOS [29] at 600K (blue) and 1173K (red). Symbols: experimental measurements in Ni and Ni-based alloys [30, 53, 54, 56].

On the contrary, with other experimental results, EELS measurements in [30, 56] indicated that bubbles were rather underpressurized. This can be explained by the low He/dpa, or temperature being too low to induce sufficient vacancy emission from bubbles to reach thermal equilibrium. The presence of hydrogen that plays a similar role as He [60, 61, 62, 63] could also contribute to the observed differences.

6. Conclusion

In the current work, parametrization of a variable-gap model for helium bubbles in nickel was presented, highlighting the difference between its version for iron. The model was then compared with experimental measurements of helium densities.

It was shown that in a FCC case, surface effect plays an important role in the Ni-Ni interaction. The observed faceting seems to be in agreement with experimental observations [1, 47, 48]. The majority of surfaces were identified as {111} and {100} planes, with surfaces of small voids having mostly {111} planes, but the surface started to be more complex, exhibiting an octahedron-like shape, with increasing size.

The model predicts helium and vacancy binding energies in a good agreement with MD values, except for a few cases of small sizes, where size (in terms of number of vacancies) is equal to their magic numbers. For these sizes, binding energies exhibit non-monotonic behavior as a function of the number of vacancies that can be hardly captured by the model, as the shape, complexity, and differences in symmetry between neighbouring sizes are approximated in a simple way. This limitation can be eliminated by using binding energy values from MD directly, as the present model is to be used in kinetic models such as CD to provide insight on nucleation and growth of bubbles in Ni and FCC metals under various He/dpa ratios. As a first approach, the model can be adopted to more complex alloys (e.g. 300 series ASS) by simply modifying elastic constants. It is expected that He-He and He-metal parts of the model would remain

globally unchanged.

CRediT authorship contribution statement

Miroslav Fokt: Writing - original draft, Investigation, Formal analysis. **Gilles Adjanor**: Writing - review editing, Supervision, Conceptualization. **Thomas Jourdan**: Writing - review editing, Supervision, Conceptualization, Methodology.

Declaration of Competing Interest

The authors declare that they have no known competing financial interests or personal relationships that could have appeared to influence the work reported in this paper.

Data availability

The raw/processed data required to reproduce these findings cannot be shared at this time due to technical or time limitations.

Acknowledgments

Appendix A. Shape analysis of bubbles' surface

The aim was to develop a method to consistently analyze shape and the surface of a bubble at the atomic scale (FCC nickel in our case). This can be a challenging problem, because a bubble - from a geometrical point of view - is a hole in the bulk. So the use of concave or convex hull algorithms could omit

some of the surface atoms, and thus underestimate or overestimate the overall volume of the bubble, respectively.

The method is based on the Wigner-Seitz defect analysis followed by the Delaunay tessellation. The first step is to identify the vacancy positions by comparing two atomic systems: a **reference state** (a perfect bulk nickel FCC lattice), and a **deformed state** (a bubble, where some atoms are missing and others are displaced due to relaxation). For each atom in a deformed state, the closest site in a reference state is found. The number of atoms (from deformed state) assigned to each atom (in reference state) is called occupancy, and can be equal to zero (vacancy), one (normal atom), or two and more (interstitial atom). In other words, one could say that occupancy is the number of atoms in a deformed state that lie within the reference state atom's Voronoi cell.

Then, in a deformed state, all helium atoms (if any) are replaced by artificial 'vacancy' atoms (atoms placed at vacancy positions), and the new configuration is tessellated using Delaunay triangulation[4], creating simplices that have vertices at atoms' positions. Surface atoms are identified as bulk vertices of simplices with one vertex as a vacancy atom. Three atoms at the bubble's surface form triangle - one face of a simplex.

This method was tested as the most reliable in terms of detecting all surface atoms with their coordinates, and surface triangles for further analysis (shape, orientation of normals). Another advantage is the detection of *true* bubble volume V_{rel} as a sum of volumes of all simplices with at least one vertex as a vacancy atom. A bubble radius is

$$r = \sqrt[3]{\frac{3V_{\text{rel}}}{4\pi}}. \tag{A.1}$$

From our perspective, this is a rigorous way to calculate a bubble's radius at the atomistic scale, as we want to be able to detect changes in a void's radius/shape when a point-defect is added. The convex hull of all surface atoms

---

[4]Python's scipy.spatial.Delaunay library based on Qhull library

379 is overestimating the final volume, and it is not sensitive enough to small size

380 changes.

Appendix B. Eshelby's inclusion for a void in anisotropic material

382 In this section, we generalize the formula giving the relaxation energy to

383 anisotropic material. Using the equivalent inclusion approach, the effect of

384 helium pressure (or surface tension) is modeled by an equivalent homogeneous

385 inclusion of eigenstrain ϵ_{ij}^*. By equating the stress within the inclusion to the

386 stress produced by helium (or surface tension), we find that

$$\epsilon_{ij}^* = \frac{-p\delta_{ij}}{(C_{11} + 2C_{12})(S_{11} + 2S_{12} - 1)} = \epsilon^*\delta_{ij}. \tag{B.1}$$

387 In this equation, δ_{ij} is the Kronecker delta, p is pressure, $C_{11} = C_{1111}$ and

388 $C_{12} = C_{1122}$ are the elastic constants and $S_{11} = S_{1111}$ and $S_{12} = S_{1122}$ are

389 terms of the Eshelby tensor [64]. It can be shown that the relaxation volume in

390 an infinite medium ΔV_∞ is

$$\frac{\Delta V_\infty}{V} = 3(S_{11} + 2S_{12})\epsilon^*, \tag{B.2}$$

where V is the actual volume. So the eigenstrain reads

$$\epsilon_{ij}^* = \frac{\Delta V_\infty}{V}\frac{1}{3(S_{11} + 2S_{12})}\delta_{ij} = \frac{\Delta R_\infty}{R}\frac{1}{S_{11} + 2S_{12}}\delta_{ij}, \tag{B.3}$$

391 with ΔR_∞ being the relaxation radius and R the actual radius in an infinite

392 medium. The energy stored in the matrix is

$$E^{\mathrm{M}} = -\frac{1}{2}\sigma_{ij}^I \epsilon_{ij}^C V, \tag{B.4}$$

where $\sigma_{ij}^I = -p\delta_{ij}$ is the stress in the inclusion and ϵ_{ij}^C is the constrained deformation in the inclusion, which is equal to

$$\epsilon_{ij}^C = S_{ijkl}\epsilon_{kl}^*. \tag{B.5}$$

We can deduce that

$$E^{\mathrm{M}} = 2\pi\frac{1 - S_{11} - 2S_{12}}{S_{11} + 2S_{12}}(C_{11} + 2C_{12})R(\Delta R^\infty)^2. \tag{B.6}$$

21

The displacement of the surface can be also calculated through

$$u_i = u_i^C = S_{ijkl}\epsilon_{kl}^*x_j, \tag{B.7}$$

which reads as

$$u_i = (S_{11} + 2S_{12})\epsilon^*x_i. \tag{B.8}$$

We can see that the displacement is isotropic, even if the material is not elastically isotropic.

For an elastically isotropic material, we have

$$C_{11} + 2C_{12} = 2\mu\frac{1+\nu}{1-2\nu}, \tag{B.9}$$

$$1 - S_{11} - 2S_{12} = \frac{2}{3}\frac{1-2\nu}{1-\nu}, \tag{B.10}$$

$$S_{11} + 2S_{12} = \frac{1}{3}\frac{1+\nu}{1-\nu}, \tag{B.11}$$

and so we obtain

$$E^{\mathrm{M}} = 8\pi\mu R(\Delta R^\infty)^2. \tag{B.12}$$

Comparing both isotropic and anisotropic cases, the equivalent shear modulus is equal to

$$\mu = \frac{1}{4}\frac{(1 - S_{11} - 2S_{12})}{S_{11} + 2S_{12}}(C_{11} + 2C_{12}). \tag{B.13}$$

References

[1] P. Maziasz, Overview of microstructural evolution in neutron-irradiated austenitic stainless steels, Journal of Nuclear Materials 205 (1993) 118 – 145, ISSN 0022-3115, URL http://www.sciencedirect.com/science/article/pii/002231159390077C.

[2] K. Fujimoto, T. Yonezawa, E. Wachi, Y. Yamaguchi, M. Nakano, R. Shogan, J. Massoud, T. Mager, Effect of the accelerated irradiation and hydrogen/helium gas on IASCC characteristics for highly irradiated austenitic stainless steels, in: proc. 12 th International Conference on Environmental Degradation of Materials in Nuclear Power Systems–Water

Reactors, ed. TR Allen, PJ King and L. Nelson, TMS, Warrendale, PA, 299, 2005.

[3] R. Simons, Helium production in fast breeder reactor out-of-core structural components, in: Effects of Radiation on Structural Materials, ASTM International, 1979.

[4] K. Fukuya, K. Fujii, H. Nishioka, Y. Kitsunai, Evolution of microstructure and microchemistry in cold-worked 316 stainless steels under PWR irradiation, Journal of nuclear science and technology 43 (2) (2006) 159–173.

[5] M. Song, K. G. Field, R. M. Cox, G. S. Was, Microstructural characterization of cold-worked 316 stainless steel flux thimble tubes irradiated up to 100 dpa in a commercial Pressurized Water Reactor, Journal of Nuclear Materials 541 (2020) 152400.

[6] K. Fujii, K. Fukuya, G. Furutani, T. Torimaru, A. Kohyama, Y. Kotah, F. Ford, G. Was, J. Nelson, Swelling in 316 Stainless Steel Irradiated to 53 dpa in a PWR, in: Proc. 10th Intl. Conf. on Environmental Degradation of Materials in Nuclear Power Systems-Water Reactors, NACE/ANS/TMS, 2001.

[7] P. J. Maziasz, Effects of helium content of microstructural development in Type 316 stainless steel under neutron irradiation, Tech. Rep., Oak Ridge National Lab., TN (USA), 1985.

[8] P. Maziasz, Void swelling resistance of phosphorus-modified austenitic stainless steels during HFIR irradiation at 300–500 C to 57 dpa, Journal of nuclear materials 200 (1) (1993) 90–107.

[9] M. Griffiths, G. Bickel, S. Donohue, P. Feenstra, C. Judge, L. Walters, W. M., Degradation of Ni-alloy components in CANDU reactor cores, in: 16th Int. Conference on Environmental Degradation of Materials in Nuclear Power Systems-Water Reactors, Asheville, North Carolina, USA, 2013., 2013.

23

[10] E. Torres, J. Pencer, D. Radford, Density functional theory-based derivation of an interatomic pair potential for helium impurities in nickel, Journal of Nuclear Materials 479 (2016) 240–248.

[11] X. Cao, Q. Xu, K. Sato, T. Yoshiie, Effects of dislocations on thermal helium desorption from nickel and iron, Journal of Nuclear Materials 417 (1) (2011) 1034 – 1037, ISSN 0022-3115, URL http://www.sciencedirect.com/science/article/pii/S0022311510010342, proceedings of ICFRM-14.

[12] J. Xu, C. Wang, W. Zhang, C. Ren, H. Gong, P. Huai, Atomistic simulations of the interactions of helium with dislocations in nickel, Nuclear Materials and Energy 7 (2016) 12–19.

[13] J. Hetherly, E. Martinez, Z. Di, M. Nastasi, A. Caro, Helium bubble precipitation at dislocation networks, Scripta Materialia 66 (1) (2012) 17–20.

[14] L. Yang, F. Gao, R. J. Kurtz, X. Zu, Atomistic simulations of helium clustering and grain boundary reconstruction in alpha-iron, Acta Materialia 82 (2015) 275–286.

[15] S. J. Zinkle, L. E. Seitzman, W. G. Wolfer, I. Energy calculations for pure metals, Philosophical Magazine A 55 (1) (1987) 111–125, doi:\let\@tempa\bibinfo@X@doi10.1080/01418618708209803, URL http://dx.doi.org/10.1080/01418618708209803.

[16] S. J. Zinkle, W. G. Wolfer, G. L. Kulcinski, L. E. Seitzman, II. Effect of oxygen and helium on void formation in metals, Philosophical Magazine A 55 (1) (1987) 127–140, doi:\let\@tempa\bibinfo@X@doi10.1080/01418618708209804, URL http://dx.doi.org/10.1080/01418618708209804.

[17] H. Trinkaus, B. Singh, Helium accumulation in metals during irradiation–where do we stand?, Journal of Nuclear Materials 323 (2) (2003) 229–242.

24

[18] K. Morishita, R. Sugano, Mechanism map for nucleation and growth of helium bubbles in metals, Journal of Nuclear Materials 353 (1) (2006) 52 – 65, ISSN 0022-3115, URL http://www.sciencedirect.com/science/article/pii/S0022311506001619.

[19] K. Morishita, R. Sugano, Modeling of He-bubble migration in bcc Fe, Nuclear Instruments and Methods in Physics Research Section B: Beam Interactions with Materials and Atoms 255 (1) (2007) 52–56.

[20] M. P. Surh, J. B. Sturgeon, W. G. Wolfer, Void nucleation, growth, and coalescence in irradiated metals, Journal of nuclear materials 378 (1) (2008) 86–97.

[21] D. Brimbal, L. Fournier, A. Barbu, Cluster dynamics modeling of the effect of high dose irradiation and helium on the microstructure of austenitic stainless steels, Journal of Nuclear Materials 468 (2016) 124–139.

[22] T. Jourdan, G. Bencteux, G. Adjanor, Efficient simulation of kinetics of radiation induced defects: A cluster dynamics approach, Journal of Nuclear Materials 444 (13) (2014) 298 – 313, ISSN 0022-3115, URL http://www.sciencedirect.com/science/article/pii/S0022311513011483.

[23] D. Xu, B. D. Wirth, M. Li, M. A. Kirk, Combining in situ transmission electron microscopy irradiation experiments with cluster dynamics modeling to study nanoscale defect agglomeration in structural metals, Acta Materialia 60 (10) (2012) 4286–4302.

[24] S. Golubov, R. Stoller, S. Zinkle, A. Ovcharenko, Kinetics of coarsening of helium bubbles during implantation and post-implantation annealing, Journal of nuclear materials 361 (2-3) (2007) 149–159.

[25] C. Ortiz, M. Caturla, C. Fu, F. Willaime, He diffusion in irradiated α- Fe: An ab-initio-based rate theory model, Physical review B 75 (10) (2007) 100102.

[26] A. A. Kohnert, B. D. Wirth, Cluster dynamics models of irradiation damage accumulation in ferritic iron. I. Trap mediated interstitial cluster diffusion, Journal of Applied Physics 117 (15) (2015) 154305.

[27] T. Jourdan, J.-P. Crocombette, A variable-gap model for calculating free energies of helium bubbles in metals, Journal of Nuclear Materials 418 (13) (2011) 98 – 105, ISSN 0022-3115, URL `http://www.sciencedirect.com/science/article/pii/S0022311511006921`.

[28] K. Morishita, R. Sugano, Mechanism map for nucleation and growth of helium bubbles in metals, Journal of nuclear materials 353 (1-2) (2006) 52–65.

[29] H. Trinkaus, Energetics and formation kinetics of helium bubbles in metals, Radiation Effects 78 (1-4) (1983) 189–211.

[30] E. Torres, C. Judge, H. Rajakumar, A. Korinek, J. Pencer, G. Bickel, Atomistic simulations and experimental measurements of helium nano-bubbles in nickel, Journal of Nuclear Materials 495 (2017) 475–483.

[31] F. Carsughi, Investigations on helium bubble structure in metals by neutron scattering and electron microscopy, Ph.D. thesis, Jlich, URL `https://publications.rwth-aachen.de/record/75152`, zsfassung in dt. Sprache; Dissertation, Rheinisch-Westflische Technische Hochschule Aachen, 1992, 1992.

[32] F. Carsughi, W. Kesternich, D. Schwahn, H. Ullmaier, H. Schroeder, Coarsening of helium bubbles in FeCrNi measured by small angle neutron scattering, Journal of nuclear materials 191 (1992) 1284–1288.

[33] S. Zhao, Y. Zhang, W. J. Weber, Stability of vacancy-type defect clusters in Ni based on first-principles and molecular dynamics simulations, Scripta Materialia 145 (2018) 71–75.

[34] E. Lee, J. Hunn, T. Byun, L. Mansur, Effects of helium on radiation-induced defect microstructure in austenitic stainless steel, Journal of nuclear materials 280 (1) (2000) 18–24.

[35] I. Chernov, A. Kalashnikov, B. Kalin, S. Y. Binyukova, Gas bubbles evolution peculiarities in ferritic–martensitic and austenitic steels and alloys under helium-ion irradiation, Journal of nuclear materials 323 (2-3) (2003) 341–345.

[36] S. Plimpton, Fast parallel algorithms for short-range molecular dynamics, Journal of computational physics 117 (1) (1995) 1–19.

[37] G. Bonny, R. Pasianot, N. Castin, L. Malerba, Ternary FeNi many-body potential to model reactor pressure vessel steels: First validation by simulated thermal annealing, Philosophical Magazine 89 (34-36) (2009) 3531–3546, URL http://dx.doi.org/10.1080/14786430903299824.

[38] D. Beck, A new interatomic potential function for helium, Molecular Physics 14 (4) (1968) 311–315, URL http://dx.doi.org/10.1080/00268976800100381.

[39] A. Stukowski, Visualization and analysis of atomistic simulation data with OVITO–the Open Visualization Tool, Modelling and Simulation in Materials Science and Engineering 18 (1) (2009) 015012.

[40] A. Jelea, Molecular dynamics modeling of helium bubbles in austenitic steels, Nuclear Instruments and Methods in Physics Research Section B: Beam Interactions with Materials and Atoms 425 (2018) 50–54.

[41] P. Vinet, J. R. Smith, J. Ferrante, J. H. Rose, Temperature effects on the universal equation of state of solids, Physical Review B 35 (4) (1987) 1945.

[42] A. A. Kohnert, M. A. Cusentino, B. D. Wirth, Molecular statics calculations of the biases and point defect capture volumes of small cavities, Journal of Nuclear Materials 499 (2018) 480–489.

[43] A. P. Thompson, S. J. Plimpton, W. Mattson, General formulation of pressure and stress tensor for arbitrary many-body interaction potentials under periodic boundary conditions, The Journal of chemical physics 131 (15) (2009) 154107.

[44] B. Uberuaga, R. Hoagland, A. Voter, S. Valone, Direct transformation of vacancy voids to stacking fault tetrahedra, Physical review letters 99 (13) (2007) 135501.

[45] R. Schibli, R. Schäublin, On the formation of stacking fault tetrahedra in irradiated austenitic stainless steels–A literature review, Journal of Nuclear Materials 442 (1-3) (2013) S761–S767.

[46] F. E. Fujita, A theory of medium range order in supercooled liquid and amorphous solid metals, in: Rapidly Quenched Metals, Elsevier, 585–588, 1985.

[47] Y. Dong, B. Sencer, F. Garner, E. Marquis, Microchemical and microstructural evolution of AISI 304 stainless steel irradiated in EBR-II at PWR-relevant dpa rates, Journal of Nuclear Materials 467 (2015) 692–702.

[48] Q. Wei, N. Li, K. Sun, L. Wang, The shape of bubbles in He-implanted Cu and Au, Scripta Materialia 63 (4) (2010) 430–433.

[49] R. Tran, Z. Xu, B. Radhakrishnan, D. Winston, W. Sun, K. A. Persson, S. P. Ong, Surface energies of elemental crystals, Scientific data 3 (1) (2016) 1–13.

[50] W.-B. Zhang, C. Chen, S.-Y. Zhang, Equilibrium crystal shape of Ni from first principles, The Journal of Physical Chemistry C 117 (41) (2013) 21274–21280.

[51] P. Bublíková, P. Halodová, M. Fokt, H. NAMBURI, V. Rosneckỳ, J. Procházka, J. Duchoň, D. Vojtěch, Neutron irradiated reactor internals: An applied methodology for specimen preparation and post irradiation

examination by electron microscopy methods, Manufacturing technology 18 (4) (2018) 545–551.

[52] K. Fujimoto, T. Tsuda, Y. Mogami, T. Matsubara, S. Yaguchi, Post-irradiation examination using TEM method for swelling evaluation of baffle plate in PWR core internals, Proceeding of 54th annual meeting of Hot Laboratories and Remote handling Working Group (HOTLAB 2017), Japan (2017) 540.

[53] G. Amarendra, B. Viswanathan, A. Bharathi, K. Gopinathan, Nucleation and growth of helium bubbles in nickel studied by positron-annihilation spectroscopy, Physical Review B 45 (18) (1992) 10231.

[54] W. Qiang-Li, Kesternich, H. Schroeder, D. Schwahn, H. Ullmaier, et al., Gas densities in helium bubbles in nickel measured by small angle neutron scattering, Acta Metallurgica et Materialia 38 (12) (1990) 2383–2392.

[55] C. Judge, H. Rajakumar, A. Korinek, G. Botton, J. Cole, J. Madden, J. Jackson, P. Freyer, L. Giannuzzi, M. Griffiths, High resolution transmission electron microscopy of irradiation damage in inconel x-750, in: Proceedings of the 18th International Conference on Environmental Degradation of Materials in Nuclear Power Systems–Water Reactors, Springer, 727–741, 2019.

[56] C. Walsh, J. Yuan, L. Brown, A procedure for measuring the helium density and pressure in nanometre-sized bubbles in irradiated materials using electron-energy-loss spectroscopy, Philosophical Magazine A 80 (7) (2000) 1507–1543.

[57] S. Fréchard, M. Walls, M. Kociak, J. Chevalier, J. Henry, D. Gorse, Study by EELS of helium bubbles in a martensitic steel, Journal of nuclear materials 393 (1) (2009) 102–107.

[58] W. Jäger, R. Manzke, H. Trinkaus, G. Crecelius, R. Zeller, J. Fink, H. Bay,

Density and pressure of helium in small bubbles in metals, Journal of Nuclear Materials 111 (1982) 674–680.

[59] W. Jäger, R. Manzke, H. Trinkaus, R. Zeller, J. Fink, G. Crecelius, The density and pressure of helium in bubbles in metals, Radiation effects 78 (1-4) (1983) 315–325.

[60] C. D. Judge, N. Gauquelin, L. Walters, M. Wright, J. I. Cole, J. Madden, G. A. Botton, M. Griffiths, Intergranular fracture in irradiated Inconel X-750 containing very high concentrations of helium and hydrogen, Journal of Nuclear Materials 457 (2015) 165–172.

[61] D. J. Edwards, F. A. Garner, S. M. Bruemmer, P. Efsing, Nano-cavities observed in a 316SS PWR flux thimble tube irradiated to 33 and 70dpa, Journal of Nuclear Materials 384 (3) (2009) 249–255.

[62] F. A. Garner, E. P. Simonen, B. M. Oliver, L. R. Greenwood, M. Grossbeck, W. Wolfer, P. Scott, Retention of hydrogen in fcc metals irradiated at temperatures leading to high densities of bubbles or voids, Journal of nuclear materials 356 (1-3) (2006) 122–135.

[63] G. Tolstolutskaya, V. Ruzhytskiy, I. Kopanets, S. Karpov, V. Bryk, V. N. Voyevodin, F. A. Garner, Displacement and helium-induced enhancement of hydrogen and deuterium retention in ion-irradiated 18Cr10NiTi stainless steel, Journal of nuclear materials 356 (1-3) (2006) 136–147.

[64] T. Mura, Micromechanics of Defects in Solids (Mechanics of Elastic and Inelastic Solids), Springer, 2nd edn., ISBN 9024732565, 1987.